

physics/0604199  
D0 Note CONF-5085 (2006)

# Alignment of the Central DØ Detector\*

André Sopczak  
on behalf of the DØ Collaboration

Lancaster University

## Abstract

The alignment procedure of the Silicon Microstrip Tracker, SMT, and the Central Fiber Tracker, CFT, is described. Alignment uncertainties and resulting systematic errors in physics analyses are addressed.

---

\*Presented at the workshop on Tracking In high Multiplicity Environments, TIME'05, Zurich, October 3-7, 2005. Proceedings *Nucl. Inst. Methods A*.

## 1. Introduction

The alignment of the  $D\emptyset$  tracking detectors is crucial for many physics analyses. The precision determination of the detector element positions improves the track reconstruction and the precision measurements at the interaction point. This is particularly important for Higgs, top and B-physics, and for an impact parameter trigger. A general overview of the  $D\emptyset$  detector [1] and operation [2] has recently been given. Figure 1 shows the central  $D\emptyset$  detector, Fig. 2 gives the positions of the barrel wafers and F-disk wedges, and Fig. 3 displays a side-view of the SMT with barrels, F-disks and H-disks.

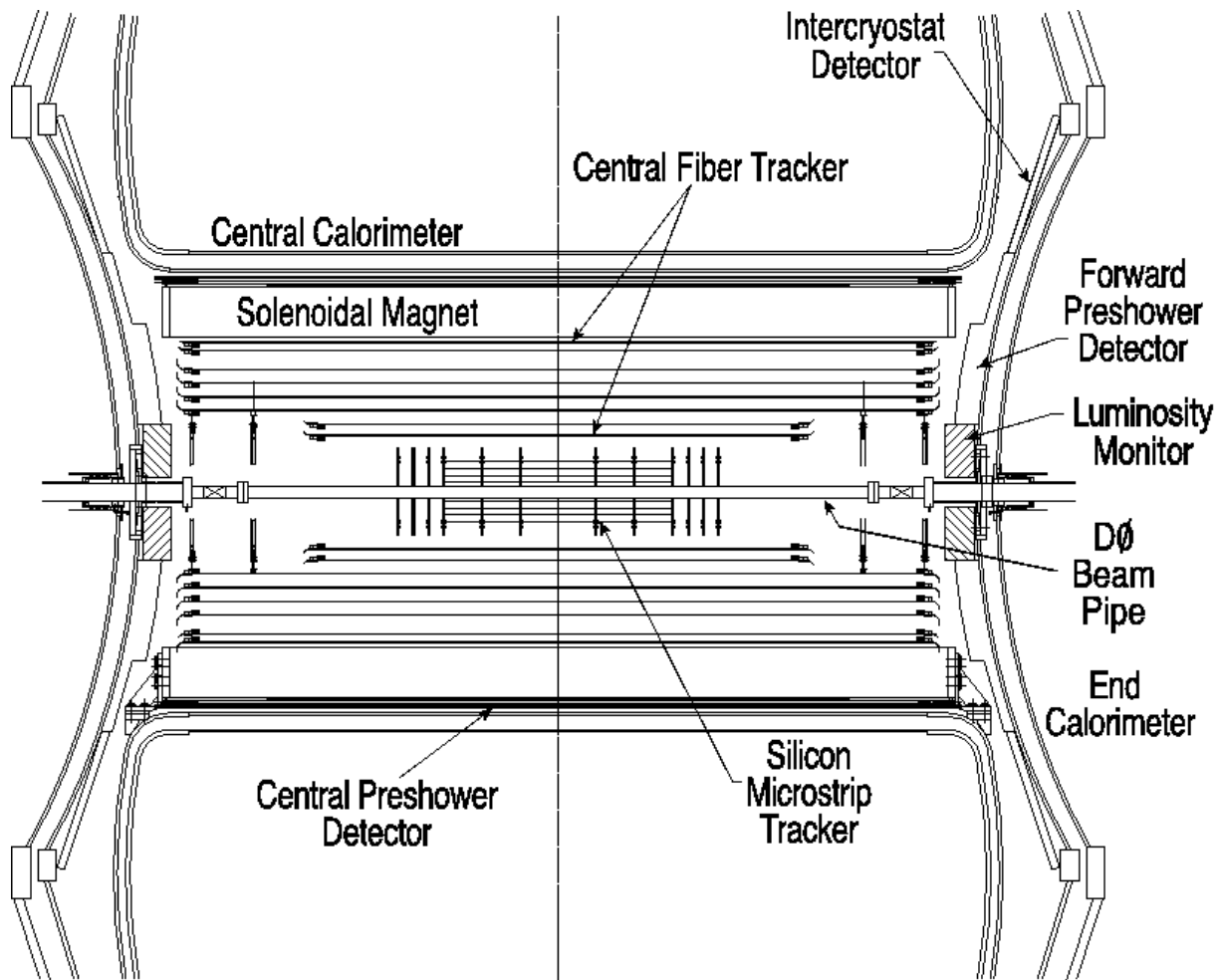


Fig. 1: Central  $D\emptyset$  detector. The Silicon Microstrip Tracker (SMT) and the Central Fiber Tracker (CFT) are used for the central tracking.

## 2. Method and alignment procedure

The basic method to align the wafers is to minimize axial-residuals and z-residuals (Fig. 4). In the SMT, there are 432 barrel wafers, 144 F-disk wedges, and 96 H-disk wedges. The CFT encompasses 304 ribbons (each with 256 parallel scintillating fibers, 1.6 or 2.5 m long). In total 976 elements require alignment. The initial position of the sensitive barrel elements were determined from metrology measurements.

The alignment procedure is as follows: a track is fitted with all hits, except the hit from the sensitive element to be aligned. Then, axial-residuals and z-residuals of the hit on the wafer to be aligned, are determined. The pull (residual/error) is calculated and the corresponding  $\chi^2$  as a sum of pulls from all tracks on the wafer are determined. The  $\chi^2$  is minimized as a function of the wafer position (three space coordinates and three angles). All wafer positions are determined and these positions serve as input geometry for the next iterative step. The iterative process continues until a convergence criterion is reached. A wafer is considered aligned if the shift divided by its uncertainty of a sensitive element between two iterations is less than a certain value. This value is called the ‘shift limit’.

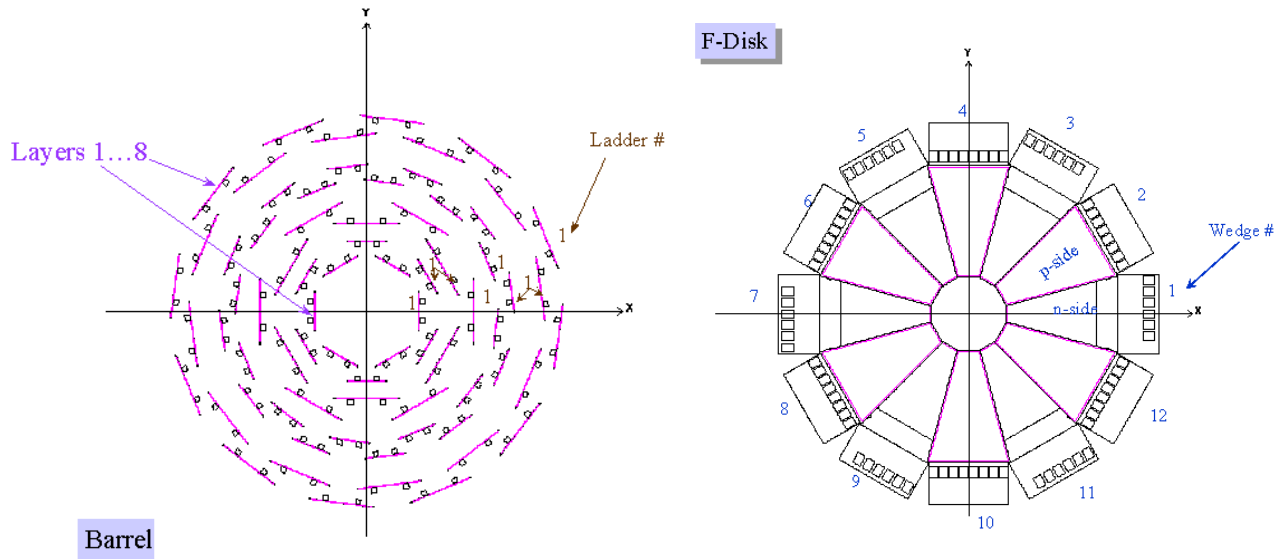


Fig. 2: Left: Barrel wafer positions. Right: F-disk wedges.

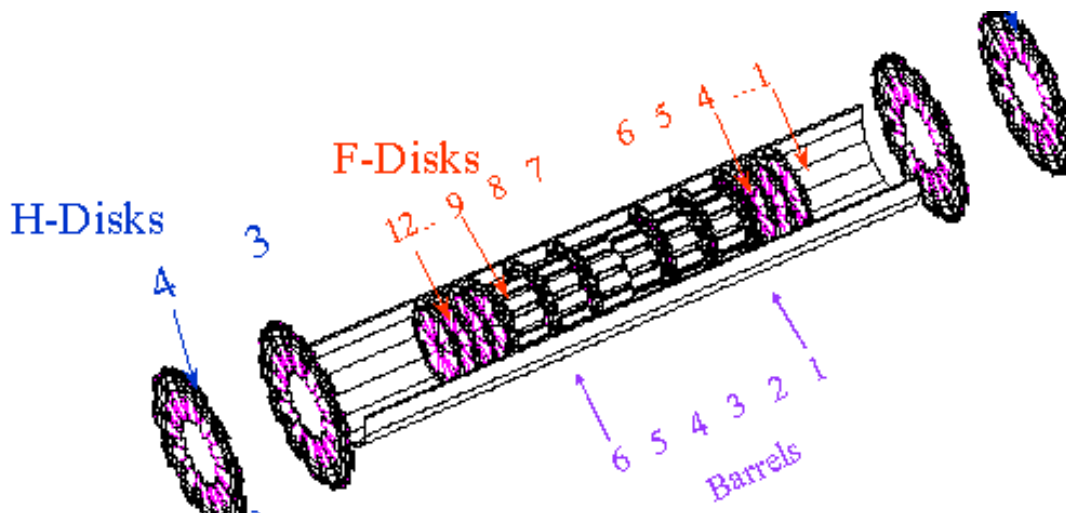


Fig. 3: SMT: Side-view of barrels, F-disks and H-disks.

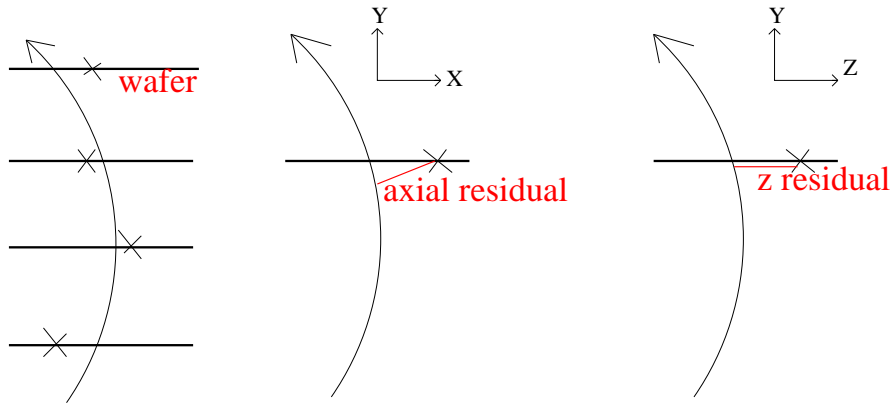


Fig. 4: Definition of axial- and z-residuals for the SMT barrel wafers as the deviations of the fitted track (curved line) from the true hit position (marked by  $\times$ ).

For the barrel, Fig. 5 shows a histogram of the number of hits per wafer for 50,000 events, and shows the shifts of each wafer between two consecutive iterations for the first and last iteration, illustrating the convergence. The corresponding plots for the F-disk and CFT are shown in Figs. 6 and 7. The number of tracks per event and the  $\chi^2$  per degree of freedom for the track reconstruction show an improvement after alignment (Fig. 8). A shift limit of 0.07 is applied.

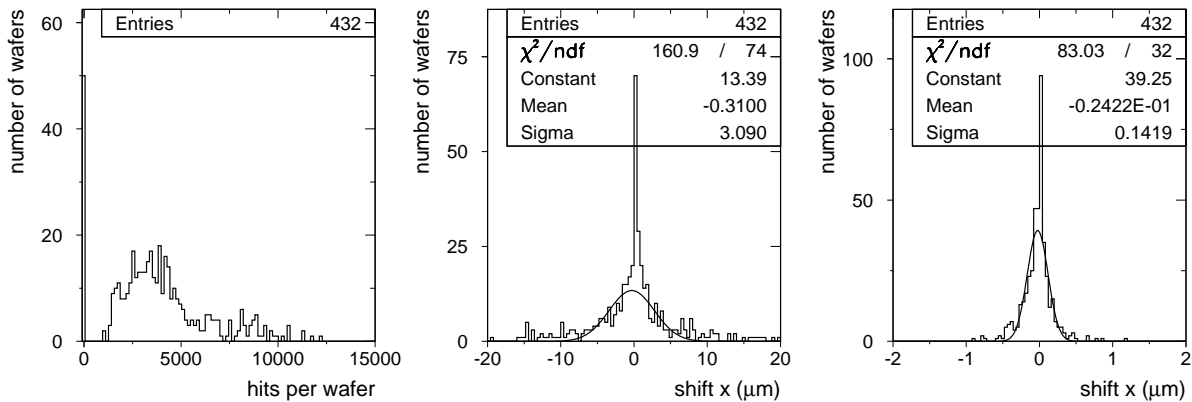


Fig. 5: Left: number of hits per wafer for 50,000 data events in the SMT barrel. Center: shifts of the 432 wafers for the first iteration. Right: shifts for the last iteration.

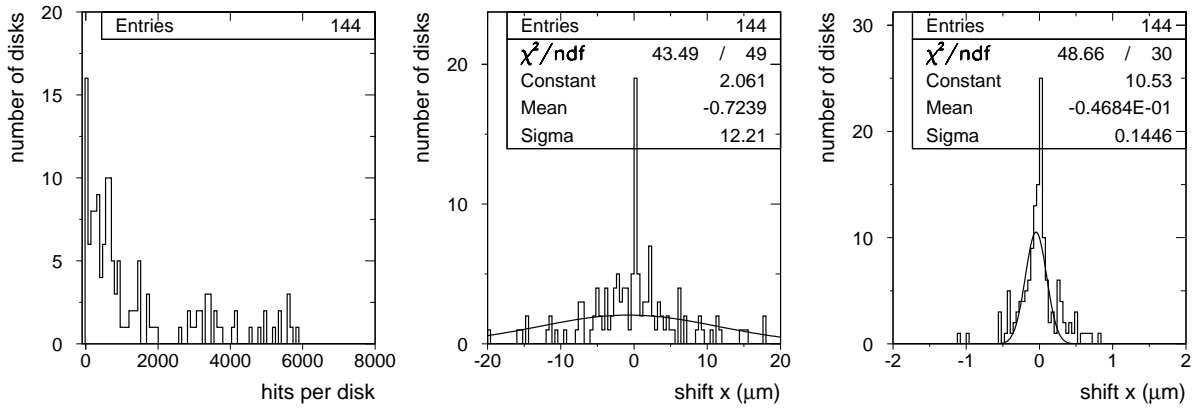


Fig. 6: Left: hits per disk for 50,000 data events for the F-disks. Center: shifts of the 144 wedges for the first iteration. Right: shifts for the last iteration.

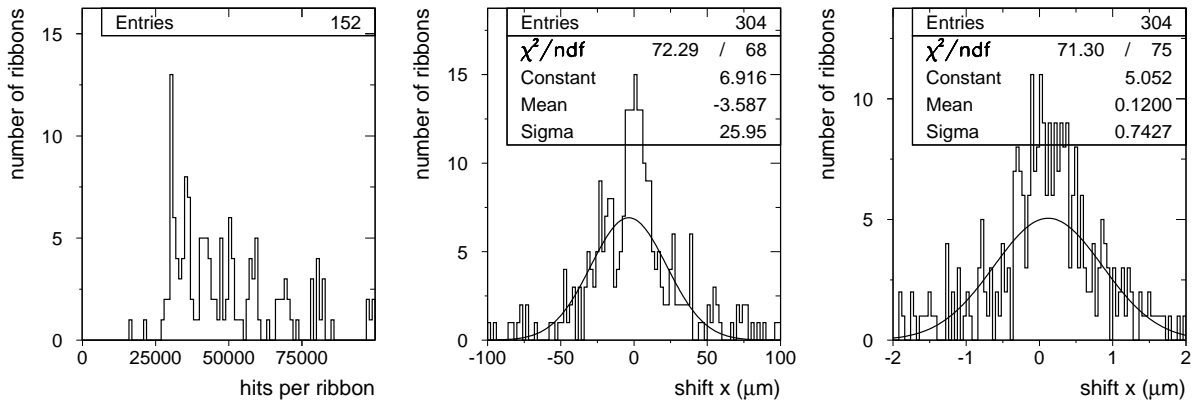


Fig. 7: Left: hits per ribbon for 50,000 data events for the CFT. Center: shifts of the 304 ribbons for the first iteration. Right: shifts for the last iteration.

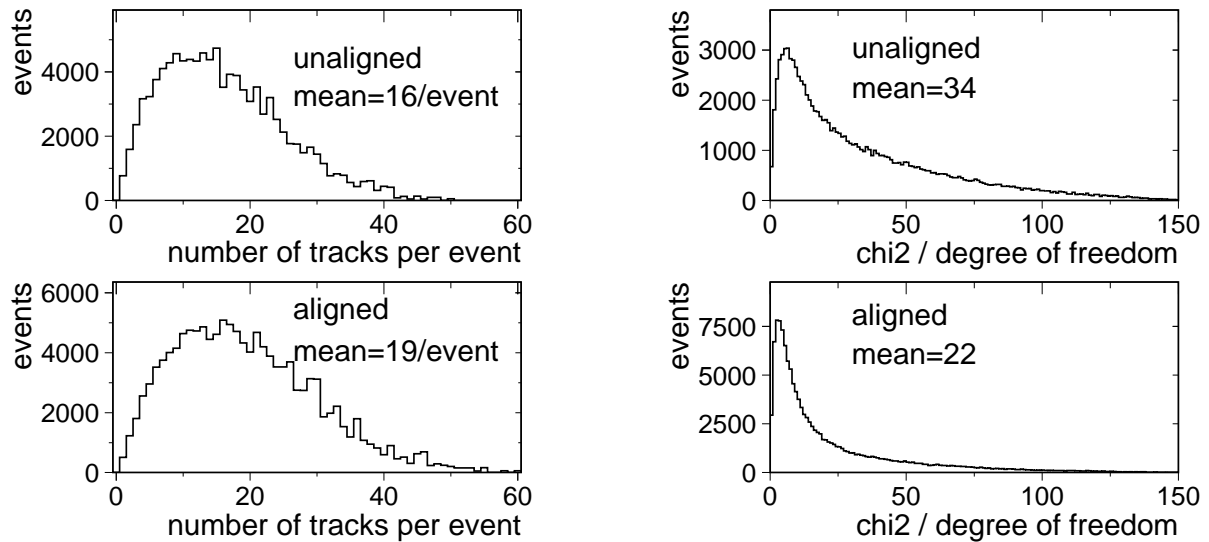


Fig. 8: Left: number of tracks per event. Right:  $\chi^2$  per degree of freedom. Both, before and after alignment.

### 3. Residuals

For the barrel, the axial residuals before and after alignment are shown for all wafers, and for each individual wafer (Fig. 9). Figure 10 shows the corresponding plots for the F-disks. The residuals in the z-direction are given in Figs. 11 and 12.

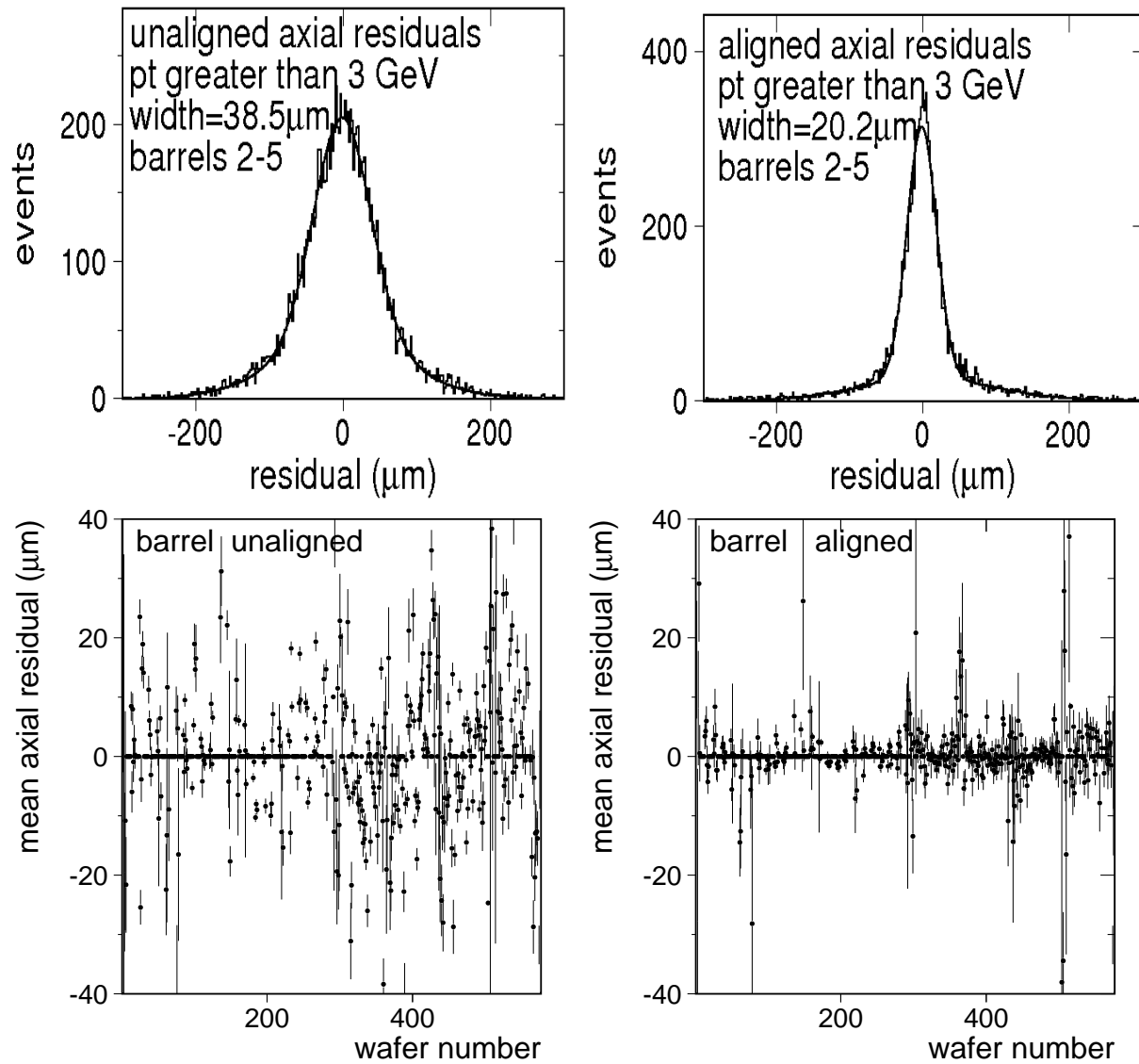


Fig. 9: Barrel axial residuals. Upper left: unaligned for all wafers. Upper right: aligned for all wafers. Lower left: unaligned for individual wafers. Lower right: aligned for individual wafers.

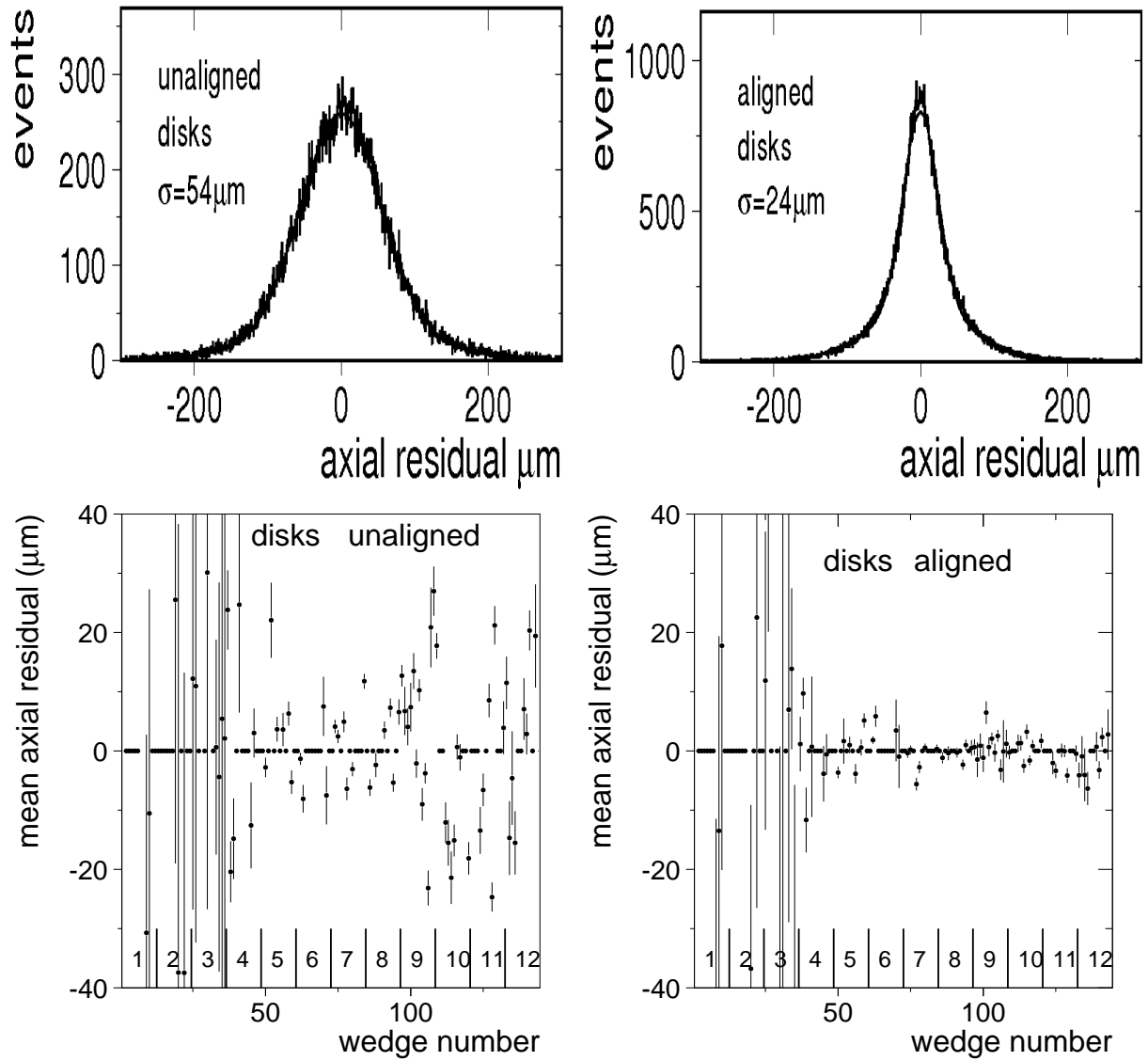


Fig. 10: F-disk axial residuals. Upper left: unaligned for all wedges. Upper right: aligned for all wedges. Lower left: unaligned for individual wedges. Lower right: aligned for individual wedges. Each of the 12 indicated disks contain 12 wedges.

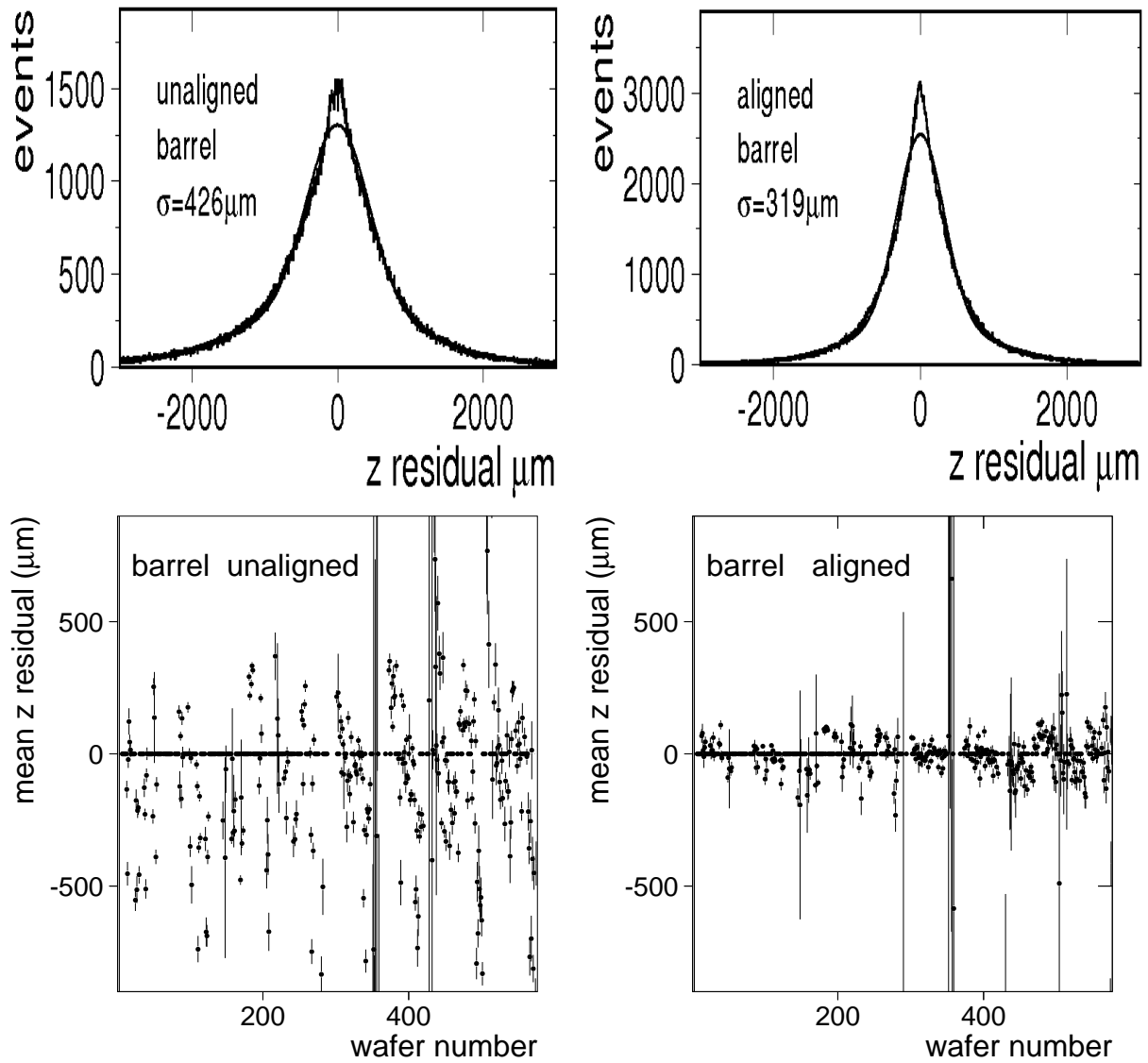


Fig. 11: Barrel residuals in the z-direction. Upper left: unaligned for all wafers. Upper right: aligned for all wafers. Lower left: unaligned for individual wafers. Lower right: aligned for individual wafers.



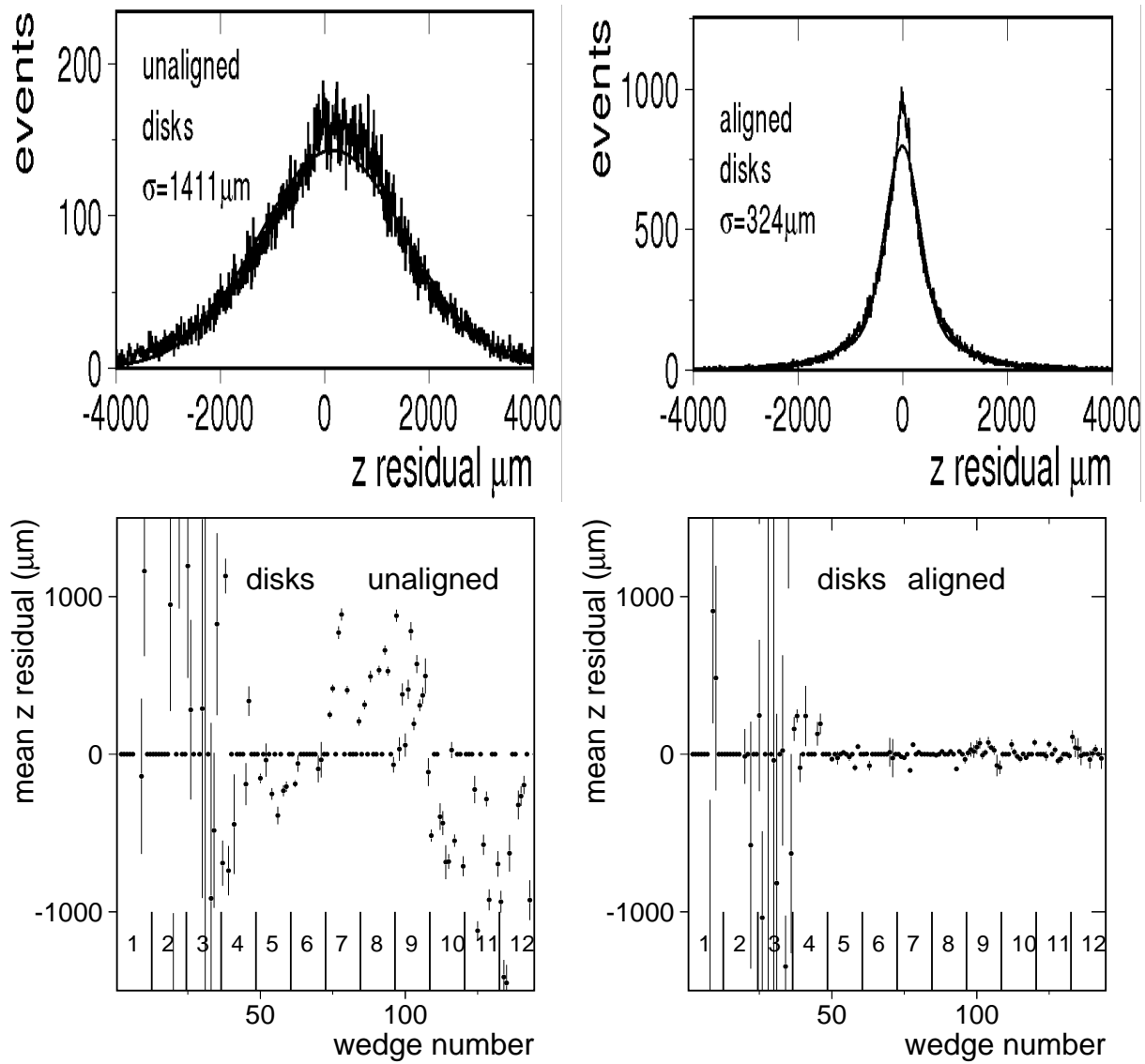


Fig. 12: F-disk residuals in z-direction. Upper left: unaligned for all wedges. Upper right: unaligned for individual wedges. Lower left: unaligned for all wedges. Lower right: aligned for individual wedges. Each of the 12 indicated disks contain 12 wedges.

#### 4. Optimization of convergence

In order to improve the alignment process, the convergence speed, the accuracy and the dependence on the number of input events have been studied. Figure 13 shows the number of wafers to be aligned as a function of the iteration number for a shift limit of 0.05. For this shift limit value no convergence is obtained. The required numbers of iterations for convergence with larger shift limits is also shown.

The variation between two aligned geometries for the same data and two different shift limits has been studied. The differences in x and y-directions between two barrel geometries for one geometry produced for shift limit 0.07, and the second one for 0.08 are shown in Figs. 14 and 15. The differences in x-direction between geometries produced with different shift limits are also shown in Fig. 14 as a function of the shift limit. For small shift limits the variation is

below  $3\mu\text{m}$ . While a very good precision of the relative wafer positions is obtained, a larger shift of the entire SMT position is possible even for a small variation of the shift limit parameter. The example in Fig. 15 shows a relative shift in y-direction of the SMT wafers with  $\sigma = 2.3\mu\text{m}$ , a very similar value as in the x-direction. However, the entire SMT is shifted between the two geometries by about  $9\mu\text{m}$ . This corresponds to an oscillating behaviour of the axial shift as a function of the wafer id.

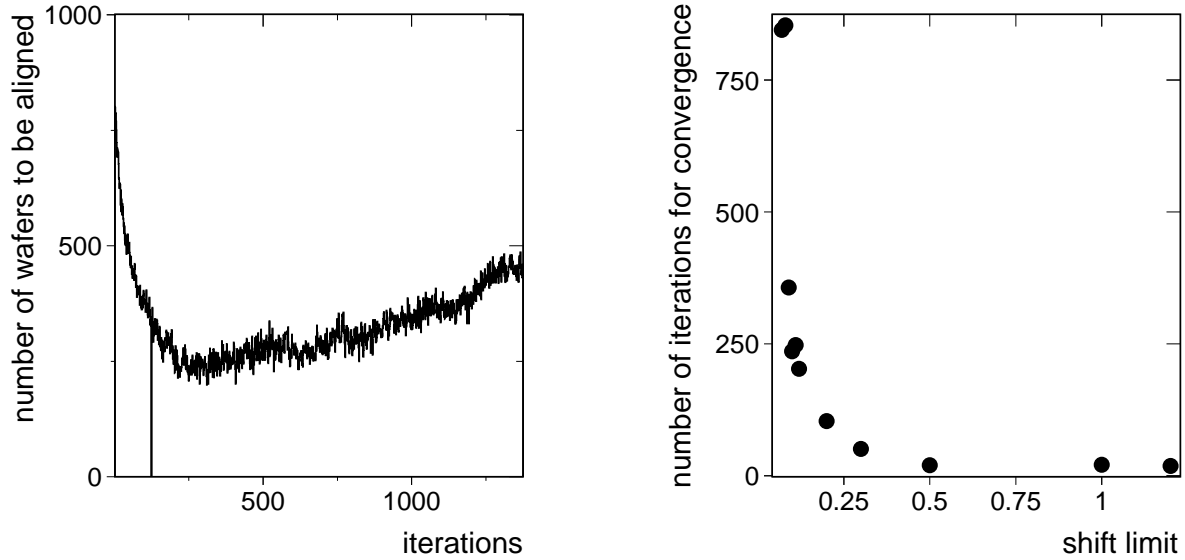


Fig. 13: Convergence of iterative process. Left: number of wafers to be aligned for shift limit 0.05 as a function of the number of iterations. The alignment process does not converge. Right: number of iterations required for convergence as a function of the shift limit in the range 0.07-1.2.

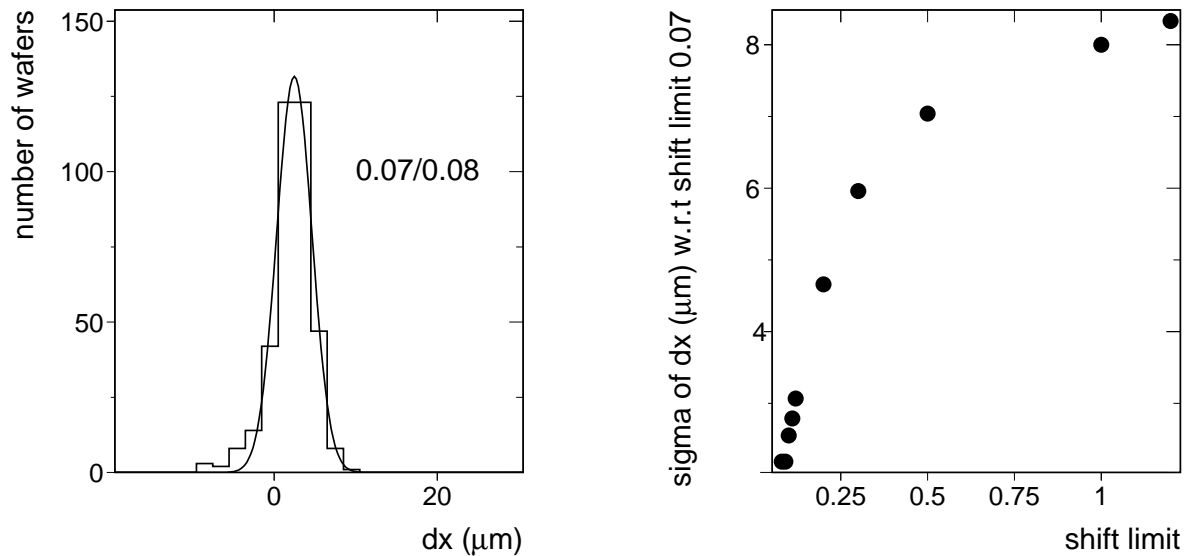


Fig. 14: Barrel difference in x-direction between aligned geometries produced with different shift-limits. Left: all wafers combined between shift limit 0.07 and 0.08. Right: as a function of the shift limit w.r.t. 0.07.

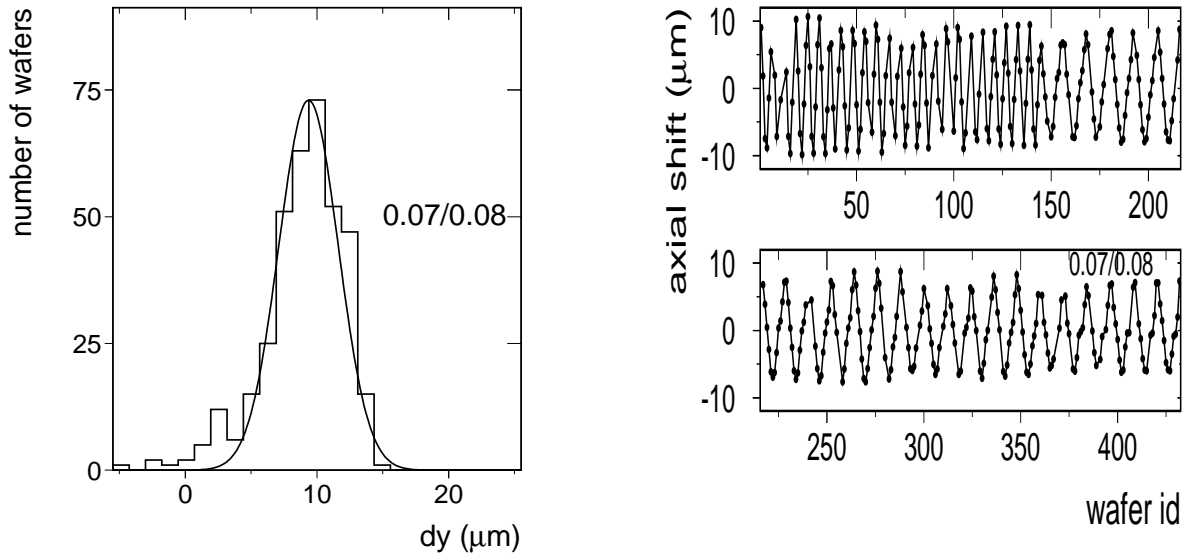


Fig. 15: Left: barrel difference in y-direction between aligned geometries produced with different shift-limits. Right: corresponding axial shift. There are 6 wafers per inner layers, and 12 per outer layers beyond wafer id 144.

In addition, the dependence of the wafer positions on the number of input events has been studied (Fig. 16). Variations of the wafer positions in the aligned geometries below  $5\mu\text{m}$  are expected for more than 30,000 data input events. In a first step the shift limit has been reduced from 0.07 to 0.05, and in a further step it has been reduced from 0.05 to 0.04. Convergence was achieved by using the aligned 0.05 geometry as starting geometry for the 0.04 run. The convergence is illustrated in Fig. 17.

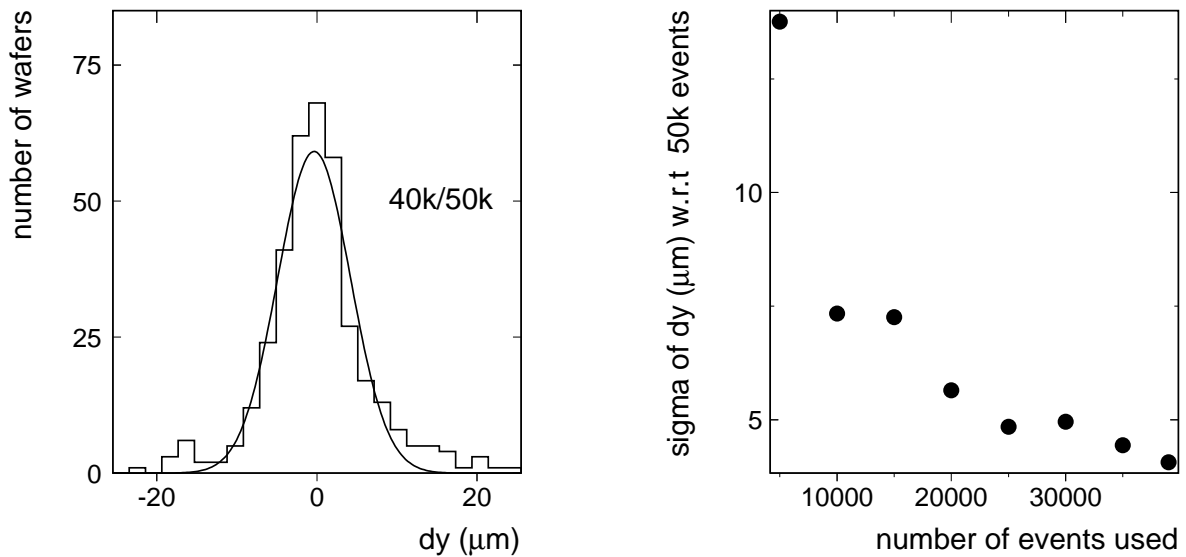


Fig. 16: Barrel difference in y-direction between aligned geometries produced with different shift-limits. Left: all wafers combined between 40,000 and 50,000 data input events. Right: as a function of the number of input events w.r.t. 50,000 events.

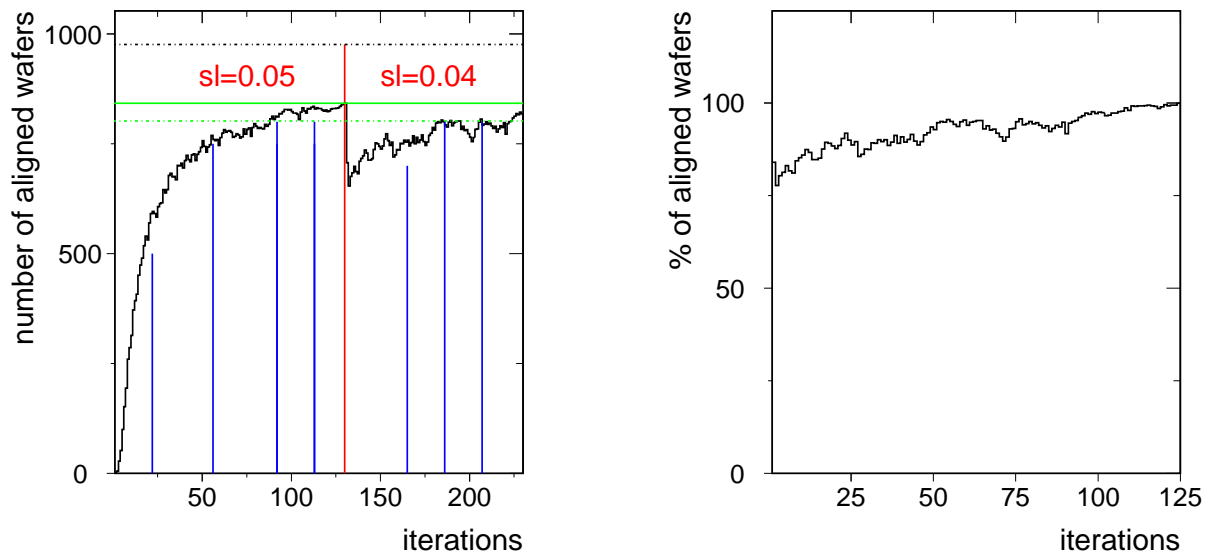


Fig. 17: Convergence of iterative process for two additional alignment steps, starting with the aligned geometry for shift limit 0.07. Left: number of aligned wafers for shift limit 0.05 and 0.04. Vertical lines correspond to 72h CPU time. Right: number of iterations required for shift limit 0.04 (in %) w.r.t. the converged 0.05 alignment.

## 5. Uncertainties from procedure variations

In order to determine the uncertainty in the alignment procedure the CFT geometries are compared for two cases a) when SMT and CFT were aligned simultaneously, and b) when the SMT was aligned first, and then the CFT was aligned. No significant effect on the alignment was observed (Fig. 18).

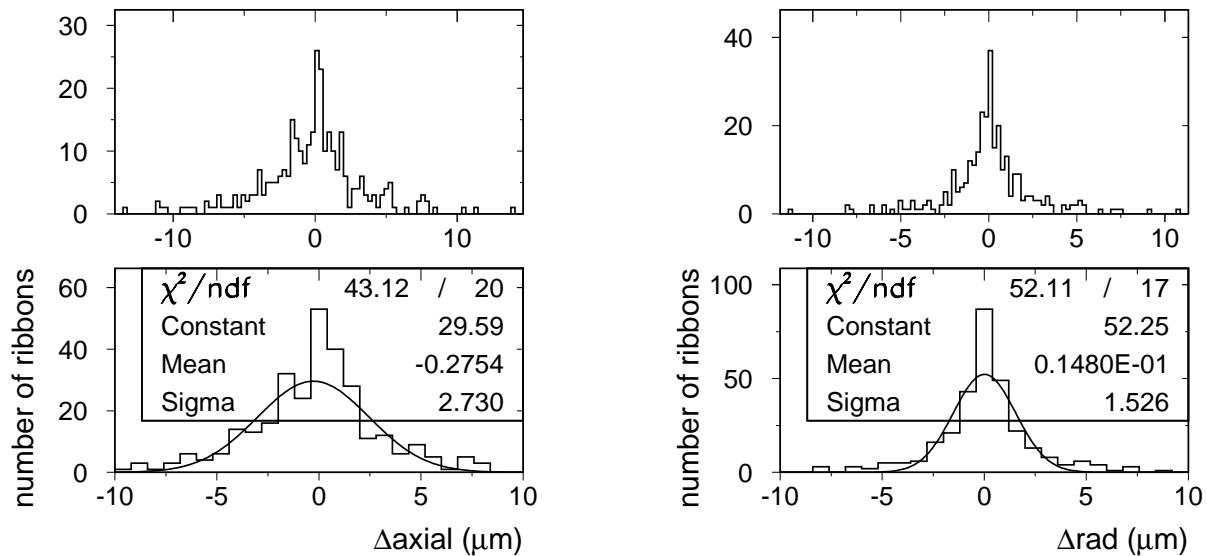


Fig. 18: Differences between geometries as explained in the text.

## 6. Single wafer re-alignment precision

Furthermore, in order to test the re-alignability and the corresponding systematic uncertainty, one wafer was misaligned by  $50\mu\text{m}$  w.r.t. the original aligned geometry, and subsequently re-aligned. Remarkably, in the first iteration of the re-alignment 432 elements were shifted. After re-alignment all elements were within  $1\mu\text{m}$  of the original position. The geometries before and after re-alignment are compared to the original geometry (Fig. 19).

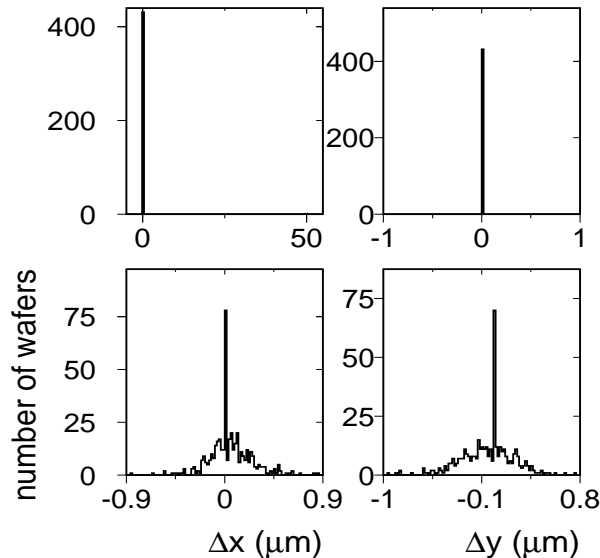


Fig. 19: Upper: one wafer is shifted  $50\mu\text{m}$  in x-direction. The other 431 wafers remain at  $\Delta x = \Delta y = 0$ . Lower: all wafers are re-aligned within  $1\mu\text{m}$ .

## 7. Longevity / variation of active elements

Figure 20 shows the variation of the number of disabled elements with time. During each data-taking shutdown several disabled elements were repaired.

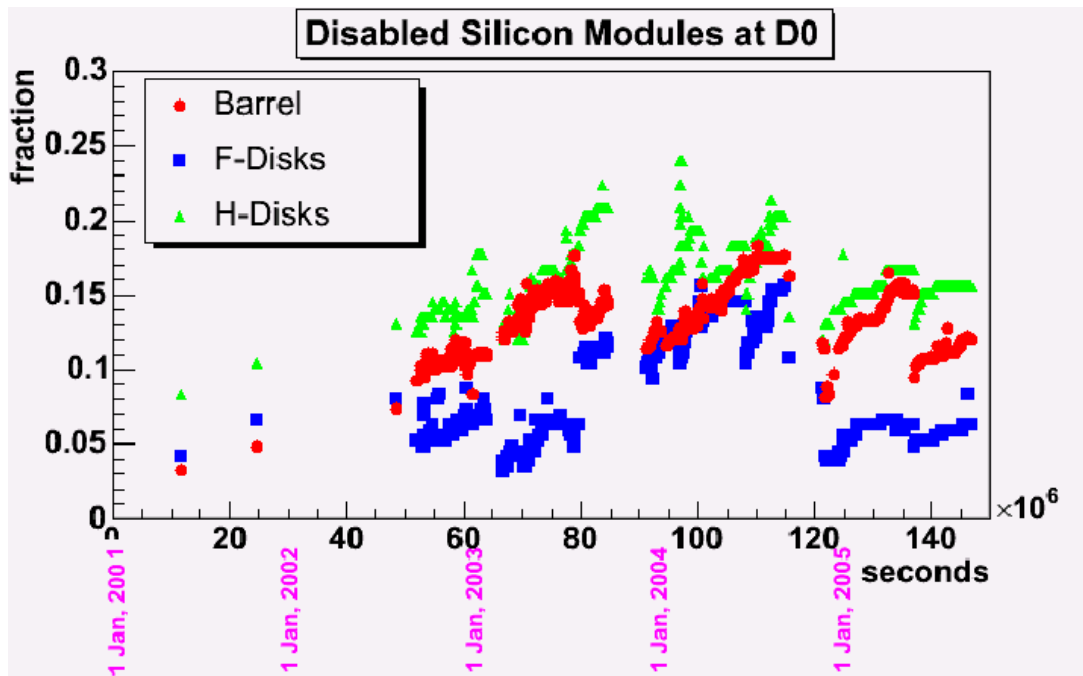


Fig. 20: Fraction of disabled elements as a function of time.

## 8. Single wafer alignment in data rerun

After data-taking shutdowns some additional wafers become operational and require alignment. Figure 21 shows an example of residuals for a single wafer (mean value of the fitted Gaussian) before and after alignment.

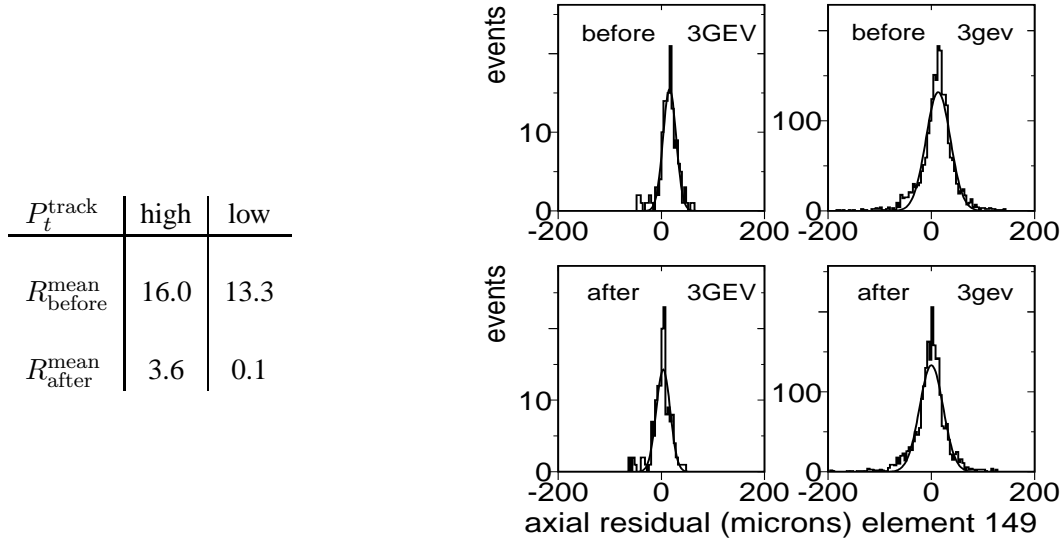


Fig. 21: Residual mean values (in  $\mu\text{m}$ ) of a single wafer (mean value of the fitted Gaussian) before and after alignment for high and low  $P_t$  tracks. GEV refers to  $P_t > 3 \text{ GeV}$  and gev to  $P_t < 3 \text{ GeV}$ .

## 9. Alignability of wafers from different runs

As some wafers are non-operational depending on the time period of data-taking, the combination of data from different time periods improves the overall alignment. Table 1 summarizes the numbers of aligned wafers for different data-taking periods.

Table 1: Number of aligned wafers in different running periods.

Period	dates	alignable wafers
B1	Oct. 24, 2002	827
B2	Oct. 24, 2002	827
A	April 20, 2003	813
C	Aug. 10, 2003	794
A+B1+B2+C	mixed	843

## 10. Time stability of detector alignment

The detector alignment has been performed for different time periods. In order to determine the alignment precision two aligned geometries from different time periods are compared. An example is given in Fig. 22 for period 1 and 5. The time stability of the detector for various time periods between April 2002 and December 2004 has been studied and no significant variation is observed (Fig. 23).

Period	dates
1 (B1,B2)	Oct. 24, 2002
2 (A)	April 20, 2003
3 (C)	Aug. 10, 2003
4 (D)	Jan. 18, 2004
5 (E)	Aug. 17, 2004
6 (F)	Dec. 18, 2004

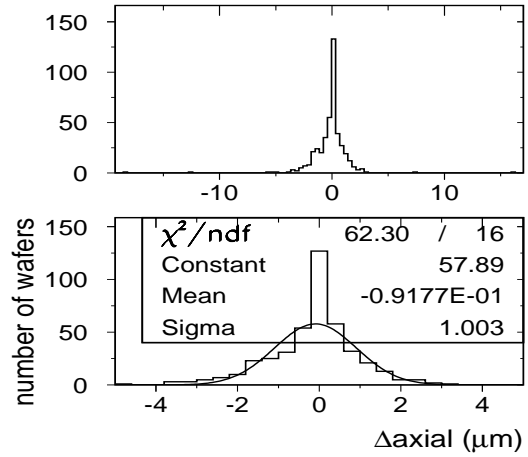


Fig. 22: Left: list of data sets and their date of data taking. Right: axial differences between wafers of the aligned geometries for time period 1 and 5. No significant variation between the aligned geometries is observed.

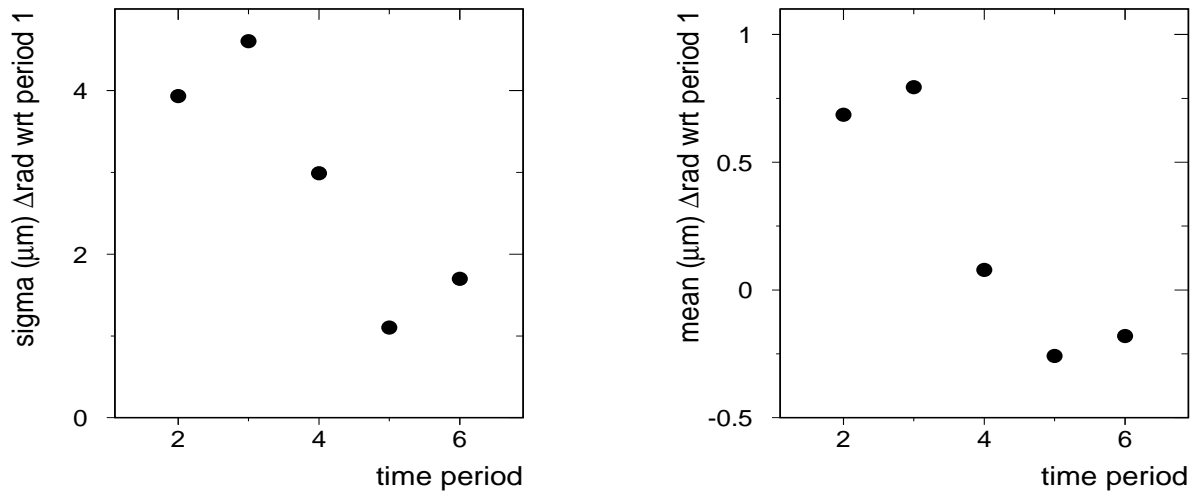


Fig. 23: Radial differences between wafers of the aligned geometries for time periods 2 to 6 w.r.t. period 1 (see Fig. 22). No significant variation between the aligned geometries is observed.

## 11. Local alignment: metrology

In addition to the previously described global alignment, where wafers are considered ideal planes with no structure, the local alignment has been investigated. Local alignment refers to the alignment on a given sensitive element. As an example, the wafer geometry and the separation in z-direction is shown in Fig. 25. Figure 24 illustrates the positions of the fiducial points on the wafers. This is particularly interesting as some wafers are made of two independent silicon plates. The precision in the distance  $\Delta z$  of two fiducial points for detector elements made of the two sensors is given in Fig. 26 from metrology. No indication of a shift in the survey between these plates is observed and variations are within  $\pm 10\mu\text{m}$ .

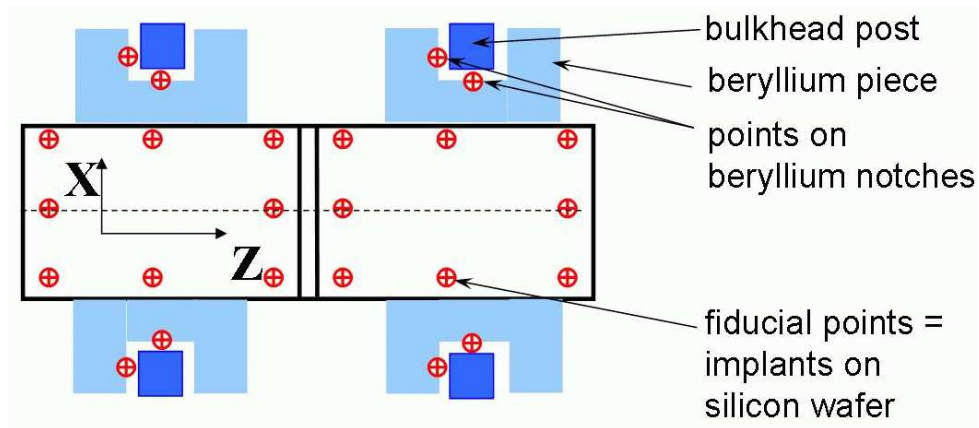


Fig. 24: Positions of fiducial points on the silicon wafers.

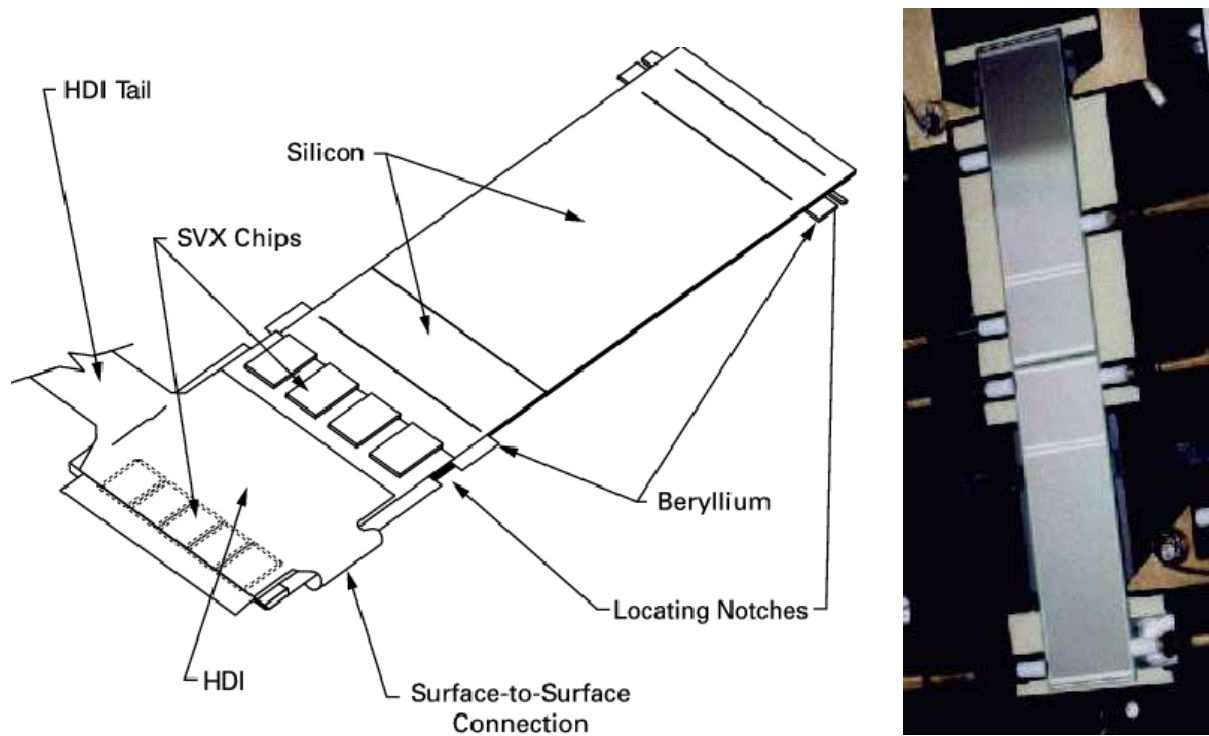


Fig. 25: Left: sensitive silicon area, HDI readout with SVX chips. Right: joining two silicon plates in support structure.



CLB minus CRA distance, microns

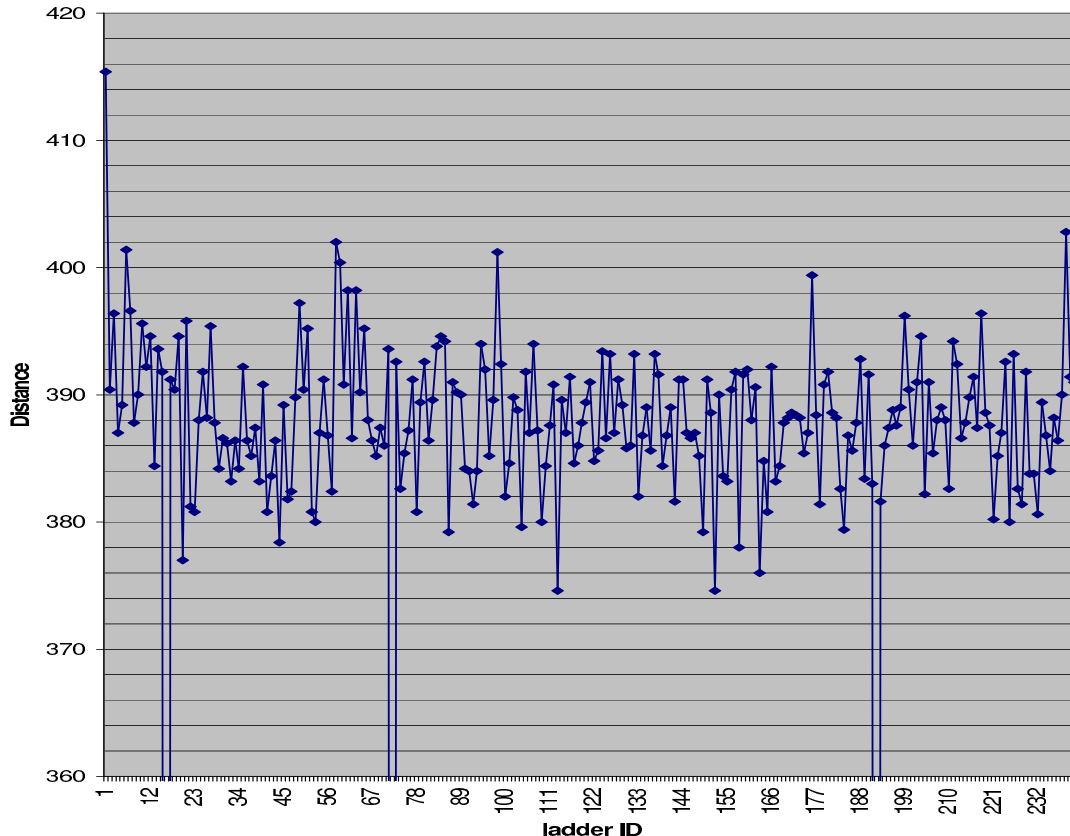


Fig. 26: Metrology z-distance measurements (in  $\mu\text{m}$ ) between two fiducial points on the joined silicon plates. No significant variation from their design position (of about  $390 \mu\text{m}$ ) is observed.

## 12. Influence on physics results

In order to determine the resolution of the Distance of Closest Approach, DCA, the position of the beamspot has been determined. A displaced beamspot position in the  $r$ - $\phi$  plane corresponds to a sine dependance of the DCA  $\delta$  as a function of the track direction  $\phi_{\text{track}}$ . It is parametrized like  $\delta = \delta_0 - P_1 \sin \phi_{\text{track}} + P_2 \cos \phi_{\text{track}}$  and this function is fitted to the data as shown in Fig. 27. The figure shows also the DCA resolution. The DCA resolution depends on the transverse momentum of the track and Table 2 gives the DCA resolutions for different  $P_t$  ranges. The DCA resolution consists of the beam-spot size convoluted with the Impact Parameter (IP) resolution. The beam-spot size is approximately  $30$ - $40 \mu\text{m}$  and depends on the machine optics.

The impact parameter resolution is crucial for the Silicon Track Trigger (STT). The beamspot determination of the previous run is used. The resulting impact parameter resolution is shown in Fig. 28.

Table 2: DCA resolution for different  $P_t$  ranges.

$P_t$ (GeV)	0.2-0.5	0.5-1	1-3	3-5	5-10	10-20	20-50
DCA res. ( $\mu\text{m}$ )	203	118	77	60	55	53	50

The impact parameter measurement is also an important aspect for b-quark tagging. Its resolution after alignment in the offline analysis together with the Monte Carlo prediction is shown in Fig. 29. Multiple scattering is the dominant source of resolution degradation at small

$P_t$  values. The figure shows also the b-quark tagging efficiency versus the light quark mistag rate.

The alignment uncertainty contributes to the systematic errors in several physics analyses. The effect of the alignment uncertainty has been studied, for example, by assuming a constant shift of  $10\mu\text{m}$  in radial direction outward (Fig. 30) in order to estimate the impact on B-meson lifetime measurements. Only a small contribution to the systematic uncertainty from alignment in B-meson lifetime measurements is observed (Table 3).

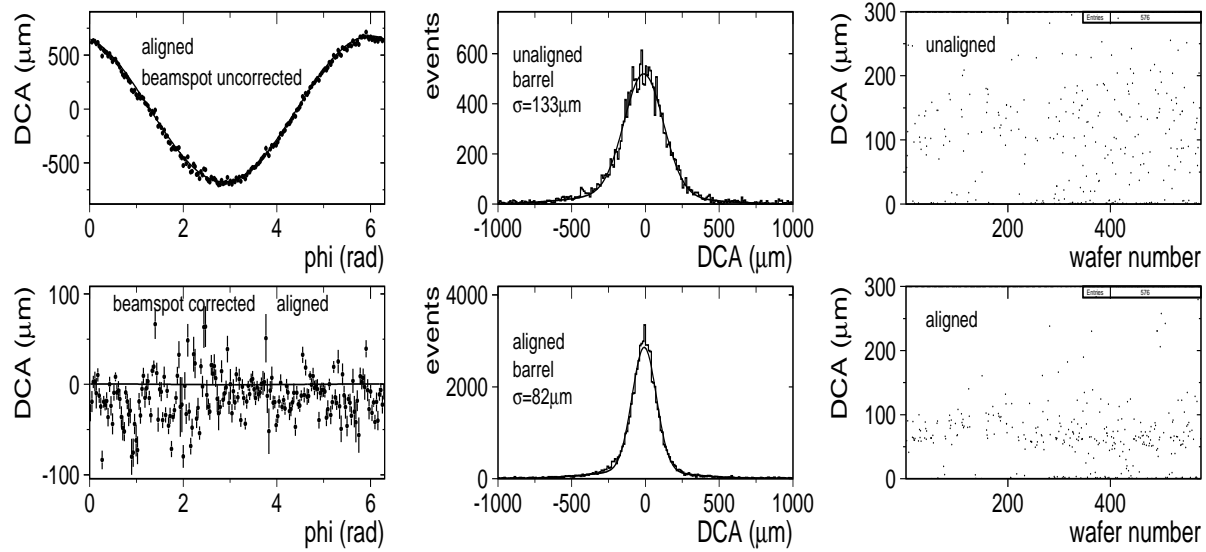


Fig. 27: Upper left: displaced beamspot position in the  $r$ - $\phi$  plane as a function of  $\phi_{\text{track}}$ . Lower left: corrected beamspot position. Center: DCA resolution for unaligned and aligned detector after beamspot correction. Right: DCA resolution for each barrel wafer.

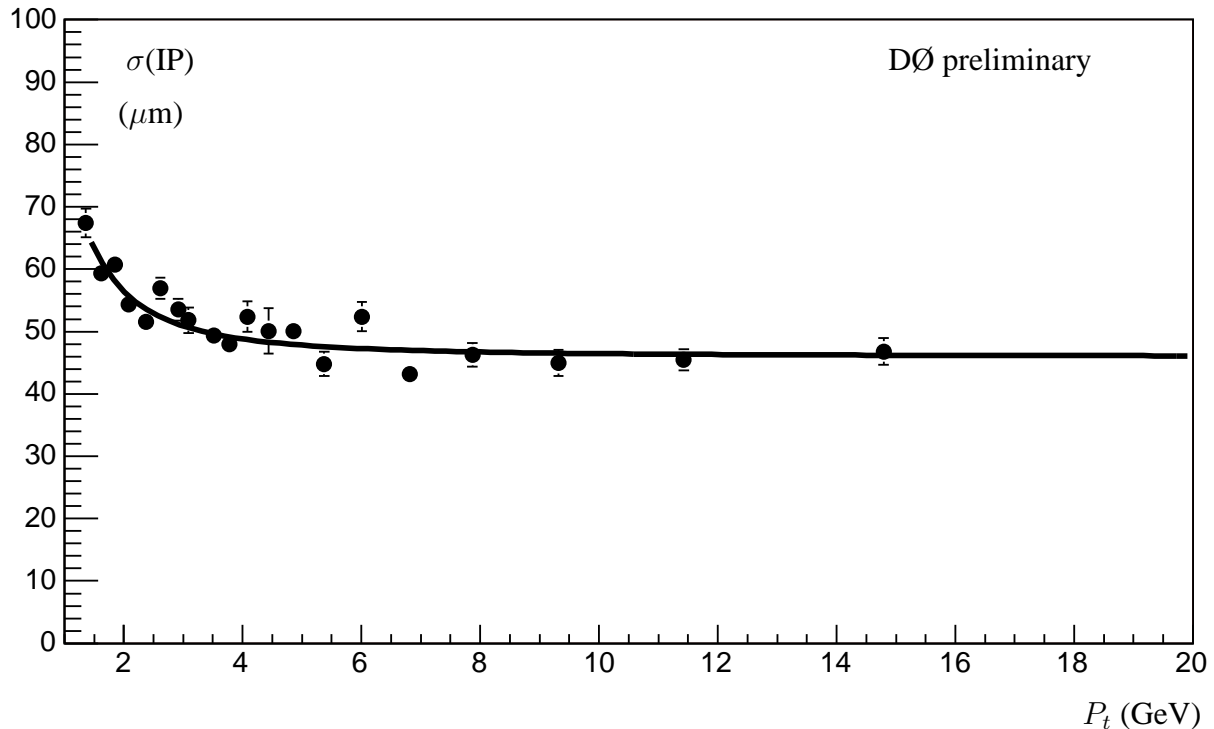


Fig. 28: Impact parameter resolution for the online Silicon Track Trigger (STT).

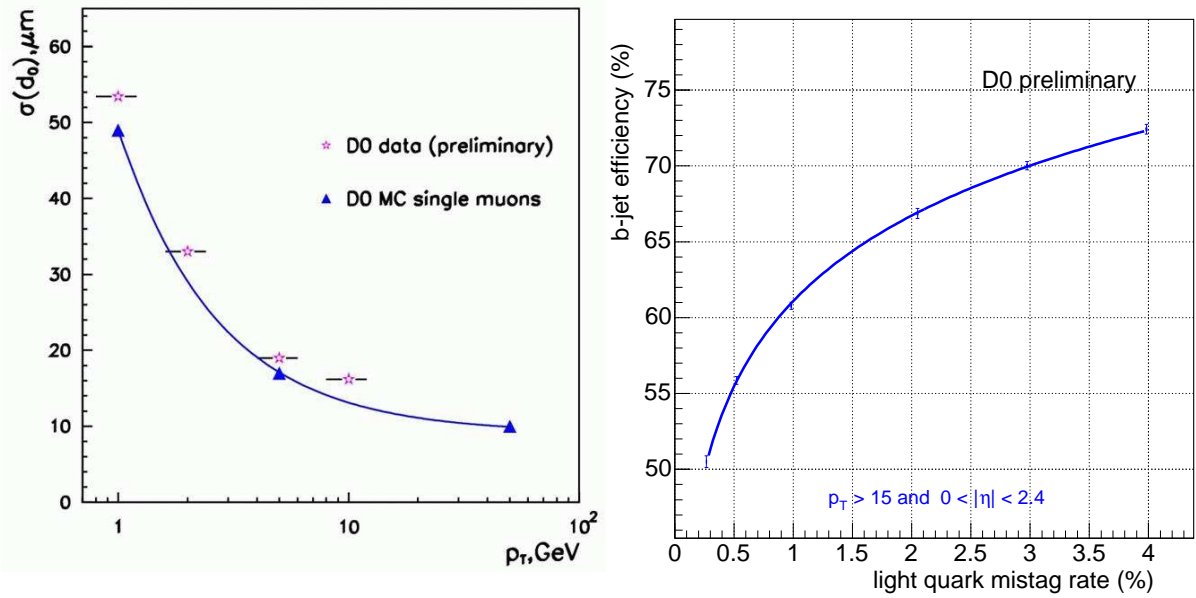


Fig. 29: Left: impact parameter resolution after alignment as a function of the transverse momentum. The beamspot size has been taken into account. Right: b-quark tagging performance using a neural network algorithm.

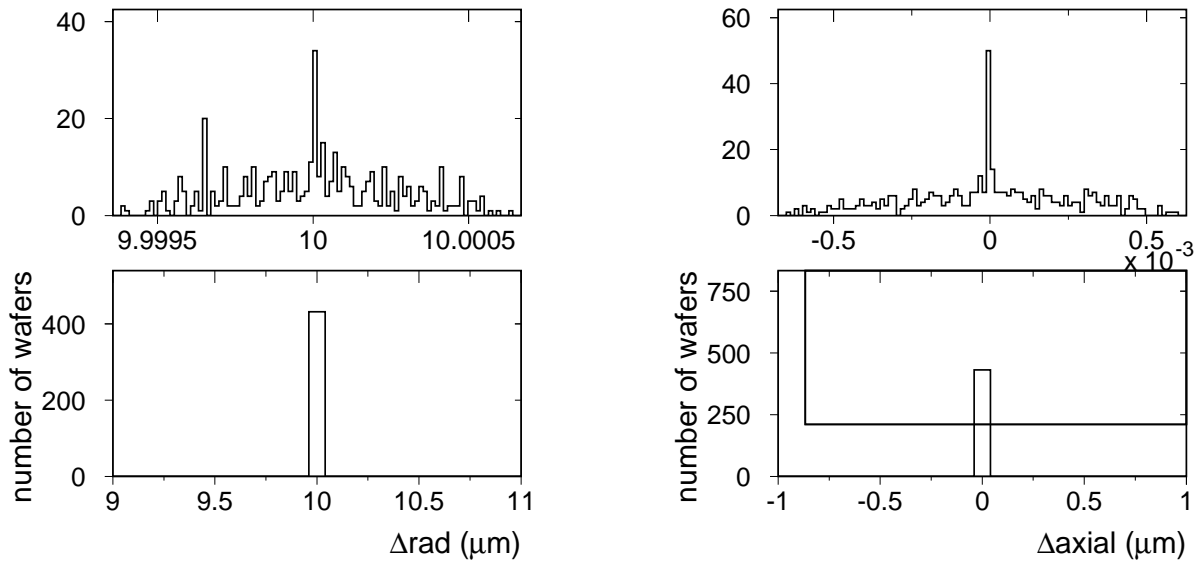


Fig. 30: For systematic error studies: comparison of geometries,  $10\mu\text{m}$  radial shift outwards.

Table 3: Systematic uncertainties  $B_s \rightarrow J/\psi\phi$  lifetime measurement.

	$c\tau(B_s)$ ( $\mu\text{m}$ )
Alignment	2
$J/\psi$ vertex	3
Model for resolution	3
Background	4
Total	6

As examples of physics analyses where the detector alignment is crucial, results from lifetime measurements are shown in Figs. 31 and 32. The signal (shaded region) is clearly visible over the background (dotted line).

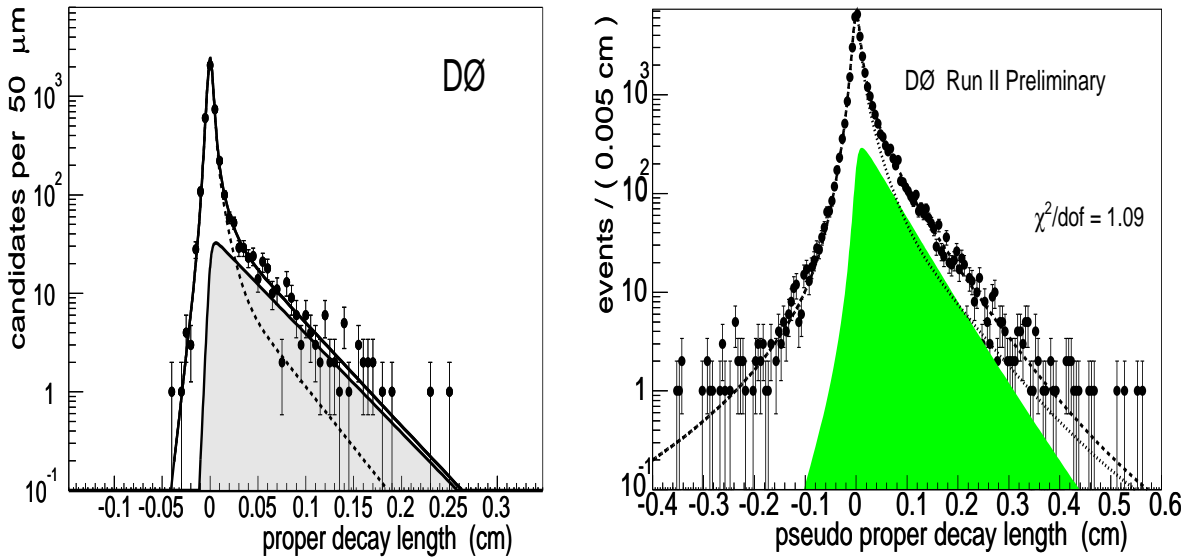


Fig. 31: B-meson lifetime measurements. Left:  $B_s \rightarrow J/\psi\phi$ . Right:  $B_s \rightarrow D_s\mu\nu X$ .

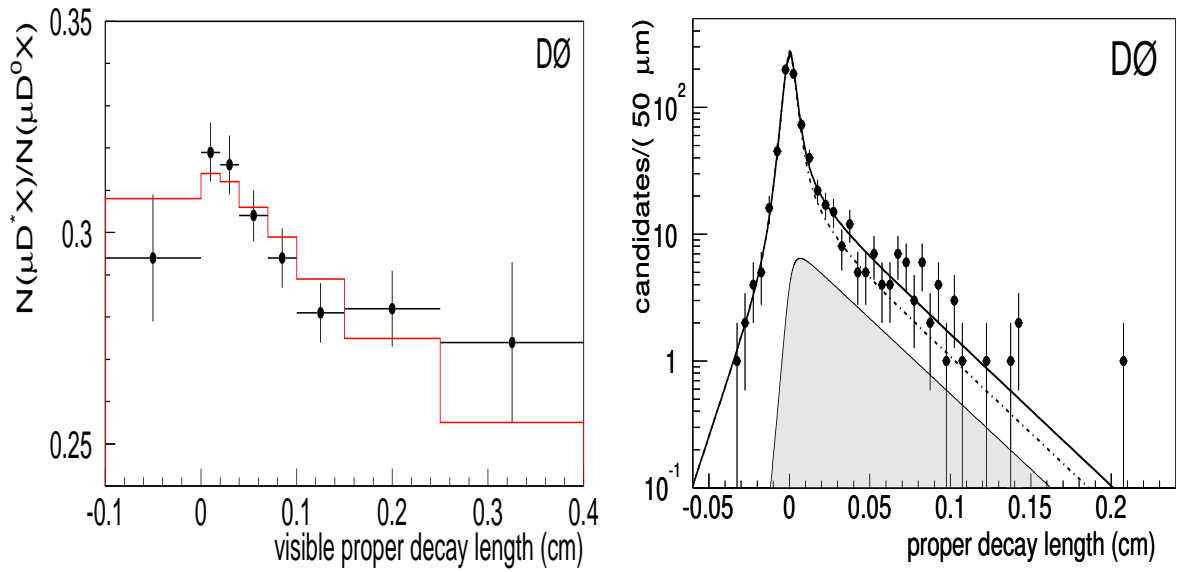


Fig. 32: Lifetime measurements. Left:  $B_d$ . Right:  $\Lambda_b \rightarrow J/\psi\Lambda$ .

### 13. Conclusions and outlook

About 850 sensitive elements have been aligned. The alignment precision is close to design value (e.g. residuals: data  $20\mu\text{m}$ , simulation  $16\mu\text{m}$ ). Some alignment parameters have been optimized. Systematic uncertainties of the alignment procedure are less than about  $10\mu\text{m}$ . The monitoring of the detector stability showed no significant movement. The alignment ensures excellent on-line and off-line b-tagging, and lifetime measurements, and is therefore crucial for Higgs, top, and B-physics. In spring 2006, a new inner layer [3], Layer-0, at 1.6 cm from the interaction point will be installed inside the current vertex detector, which will significantly improve the impact parameter resolution, as illustrated in Fig. 33.

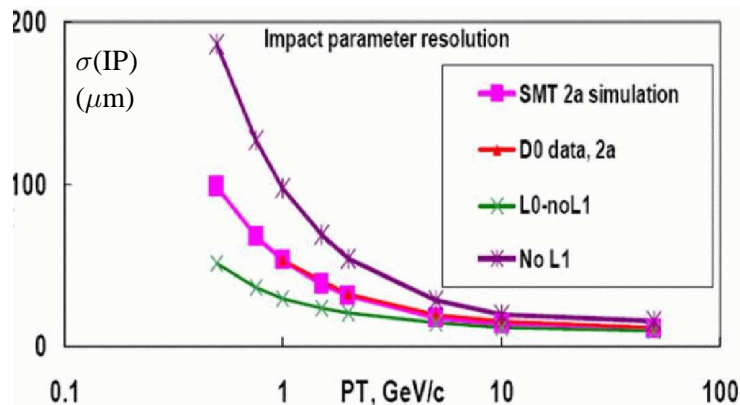


Fig. 33: Expected layer-0 (L0) improvement for the impact parameter (IP) resolution. Simulation and data (2a) overlap. Also shown is the impact parameter resolution without layer-1.

### References

- [1] DØ Collaboration, physics/0507191, submitted to *Nucl. Inst. Methods A*, “The Upgraded DØ Detector”.
- [2] R. Lipton, “DØ Tracking – From the Inside Looking Out”, these proceedings.
- [3] M. Weber, “A New Inner Layer Silicon Strip Detector for DØ”, these proceedings.

### Acknowledgements

I would like to thank the organizers of the TIME’05 conference for their kind hospitality, and Tim Brodbeck, Aran Garcia-Bellido, Mike Hildreth, Alex Melnitchouk, Ulrich Straumann, Mike Strauss and Rick van Kooten for comments on the manuscript. Contributions from Guenadi Borrisov and Brian Davies are particularly acknowledged.